Texture formation in W-type hexaferrite by cold compaction of non-magnetic interacting anisotropic shaped precursor crystallites

Cecilie G. Knudsen[a], Mathias I. Mørch[a] & Mogens Christensen[a*]

[a] Department of Chemistry & iNANO, Aarhus University, Aarhus C-8000, Denmark

* Corresponding author: mch@chem@au.dk

ABSTRACT

Crystallites of the W-type hexaferrites, $Sr(Ni_{1-x}Zn_x)_2Fe_{16}O_{27}$ (x = 0, 0.5, 1) have been aligned without applying magnetic field nor hot compaction, but through a simple synthesis process taking advantage of easy alignment of non-magnetic interacting, anisotropic-shaped precursor crystallites of goethite. The goethite precursor was prepared through a simple hydrothermal synthesis route, forming lathlike crystallites with apparent dimensions of 23.3 x 40.1 x 11.0 nm^3 as extracted from powder X-ray diffraction along the *a*-, *b*- and *c*-axis, respectively. The calcined pellets consisted of almost phase pure W-type hexaferrites with relative small impurities of spinel ferrite (≤9.02(3) wt.%). The high synthesis temperature resulted in large crystallites, which in turn caused low coercivities ($H_c \leq 5.4(1)$ kA/m) and a squareness ration (M_r/M_s, remanence (M_r) over saturation magnetisation (M_s)) close to zero for all samples. The vanishing coercivity makes M_r/M_s an unsatisfying measure of preferred orientation. Quantitative texture analysis of the samples was carried out based on 2D transmission synchrotron diffraction data collected at different orientations of the samples. The texture investigations revealed alignment of the crystallites with the *c*-axis normal to the pressing surface of the pellets. The $SrNi_2Fe_{16}O_{27}$ sample showed the highest texture index of 7.5 r.m.d^2.

KEYWORDS

W-hexaferrites, hexaferrites, goethite, magnets, cold-compaction, texture, texture-preservation, quantitative texture analysis,

1 INTRODUCTION

The world as we know it today would not function without magnetic materials, it is crucial for the development of modern and green technology. Magnets are crucial in the inter-conversion between kinetic and electric energy and is used in everything from large wind turbines to electrical toothbrushes as well as in information storage on hard disk drives.[1,2]

Different materials are used as permanent magnets. Varying from the stronger permanent magnets containing rare earth elements e.g., $Nd_2Fe_{14}B$ to the widely used magnetic material, M-type hexaferrite, MHF, ($AFe_{12}O_{19}$, A: Sr^{2+}, Ba^{2+}). The benefits of hexaferrites are that the materials are more accessible, cheaper, easier to produce and corrosion resistant.[3] Sr-hexaferrite is besides interesting because of its non-toxicity compared to Ba-hexaferrite.[4] In addition, no rare earth elements are used, which are advantageous as there have been geopolitical issues causing, supply chain problems and export quotas restrictions in the past.[5,6] Improving the magnetic performance of hexaferrites are therefore highly interesting as it could reduce reliance on rare earth elements and lead to wider applications of hexaferrites.

The magnetic performance of a permanent magnet is determined by the hysteresis loop. The properties: saturation magnetisation (M_s), coercivity (H_c), and remanence (M_r), can all be understood by studying the magnet at different length scales. On the atomic scale, the crystal structure and position of atoms with unpaired electrons are crucial for the obtainable high value of M_s. On the nanoscale, the size of the crystallites is important to control as too small and too large crystallites result in reduced H_c.[7,8] On the micrometre scale, an important factor is how well the crystallites align. If the [00*l*] directions of all crystallites are well aligned, a high M_r/M_s ratio is possible, while according to Stoner-Wohlfarth single domain, non-interacting randomly oriented spherical crystallites will have $M_r/M_s = 0.5$.[9] The ratio is therefore often used as the degree of preferred orientation, but it only applies to non-interacting,

magnetic particles where the state of magnetisation is changed by coherent rotation of the magnetic moments instead of domain wall motion.

To obtain good magnetic properties for the hexaferrites, the production today consists of high temperature reactions, size reduction by ball-milling, and alignment in magnetic fields to obtain the wanted magnetic properties. Recent research has demonstrated a bottom-up synthesis approach to production of hexaferrites with promising results. The magnetic properties of MHF-magnets are improved by controlling shape, size, and alignment through choice of synthesis and compaction.[7,10,11] Improvement of M-type hexaferrite properties have been demonstrated, however, the maximum saturation magnetisation for $SrFe_{12}O_{19}$ is 74.3 Am^2kg^{-1}.[12]

In the pursuit for materials with higher M_s than $SrFe_{12}O_{19}$ other hexaferrite structures can be considered *e.g.* X- and W-type. The unit cell of W-type hexaferrite, $AM_2Fe_{16}O_{27}$, A: Sr^{2+}, Ba^{2+}, and M: divalent cation (WHF) is illustrated in Figure 1, where different sites are marked with different colors. The structure is similar to MHF and can be described using the R and S nomenclature described in the review of the different hexaferrite structures by Pullar.[3] The R block contains the alkaline earth metal and the S block bears similarities with the spinel phase. The unit cell of WHF can be described by SSRS*S*R*, where * representing a rotation of the block through 180° around the *c*-axis, compared to MHF the unit cell is described by SRS*R*. The additional S layer opens for a wider tunability of WHF.

Saturation magnetisation: The wide tunability of the WHF originate from the choice of cations and M inserted into the structure. The highest reported M_s at room temperature obtained for WHF is 91 Am^2kg^{-1} for the structure of $SrZnLi_{0.5}Fe_{16.5}O_{27}$.[13] The specific cation site occupation fraction is crucial as it results in different saturation magnetisation values.[14] This makes the $M = Zn^{2+}$ structure interesting, because Zn^{2+} is $3d^{10}$ and it occupies the $4e_{tet}$ site and $4f_{tet}$ site, where the magnetic ordering is

antiparallel. Inserting Zn^{2+} into the tetrahedral site leads to an increase in the net magnetic moment due to the fact that Zn^{2+} has no unpaired electrons resulting in a zero atomic magnetic dipolar moment.

Coercivity: The high magnetocrystalline anisotropy, H_a, of WHF, similar to that of MHF, makes it possible to obtain coercivity in the samples. The high calcination temperatures necessary to form WHF often results in exaggerated crystal growth and consequently vanishing H_c. Attempts have been made to improve H_c through different methods as site substitution of cations and microstructure controlment.[13,15,16] The highest $H_c = 290.5$ kAm^{-1} has been measured for $Sr_{0.9}Ca_{0.1}Zn_2Fe_{16}O_{27}$.[15]

Preferred orientation: Other authors have reported oriented samples of WHF using a magnetic field, here the orientation is evaluated based on high M_r/M_s.[17,18] In samples without coercivity, which is often the case for WHF, no or low coercivity makes it impossible to study the alignment through the M_r/M_s. Simple observations of suppression of reflections and comparing the sum of intensities of (00*l*) reflections with all (*hkl*) reflections from a powder diffraction pattern make it possible to qualitatively identify, if the sample is aligned,[19] but it is not sufficient to give a quantitative texture description.

Quantitative texture analysis: Collection of transmission synchrotron 2D-data at different sample rotations allow for a quantitative texture model along with the possibility to obtain information about the crystal structure and crystallite sizes in a single experiment. This method is highly interesting as an independent alternative to give information about texture in cases where large crystallites result in low M_r/M_s and therefore cannot be used as a measure of preferred orientation. Further on, this method is also interesting in cases where classical pole figures are difficult to obtain due to massive peak overlap as in the case of the large unit cell of hexaferrites or in the case where the sample consists of small crystallites resulting in excessive peak broadening.

The aim of this paper is to use a simple synthesis route for preparing highly aligned W-type hexaferrite. Quantitative texture is extracted from 2D transmission diffraction images and reveal the simple

synthesis method is capable of preparing highly aligned samples. Furthermore, we demonstrate that the squareness ratio M_r/M_s is not good number for describing texture in samples where the coercivity is vanishing. The samples are prepared by cold-compacting and calcination of a precursor consisting of goethite (α-FeOOH), strontium carbonate ($SrCO_3$), zinc-oxide (ZnO), and/or nickel-oxide (NiO). The method takes advantage of the anisotropic shape and non-magnetic interacting crystallites of goethite. The method has earlier been reported as a simple, easy, and green solution to prepare and create texture in MHF.[20,21] The samples have been investigated using in-house powder X-ray diffraction (PXRD) and transmission synchrotron diffraction. Synchrotron measurements by multiple sample orientations was treated using the Material Analysis Using Diffraction (MAUD)-software[22], which allowed for a full texture analysis using the E-WIMV model.[23] The magnetic properties were characterized by Vibrating Sample Magnetometry (VSM).

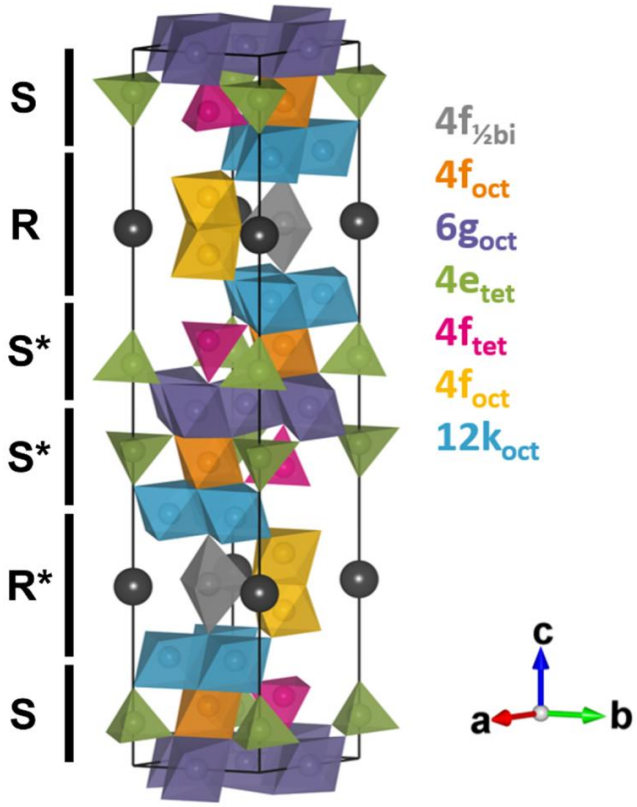

Figure 1: Unit cell of $AM_2Fe_{16}O_{27}$. Different colors indicate different sites in the structure. The position of A: Sr^{2+}, Ba^{2+} is indicated by dark grey spheres. Oxygen atoms at the corners of polyhedra are not shown. Figure prepared using VESTA.[24]

2 EXPERIMENTAL METHODS

2. 1 Precursor preparation

α-FeOOH-synthesis

The α-FeOOH precursor was prepared from $Fe(NO_3)_3 \cdot 9H_2O$ (Sigma Aldrich, ≥98%) employing a hydrothermal synthesis route. Here, 40 mL of a 1.0 M $Fe(NO_3)_3$ solution was kept under constant stirring, while 20 mL of a 8.0 M NaOH solution was added dropwise over 2 h to form a homogeneous, dark brown-reddish precipitate and kept stirring for 30 min after addition of NaOH. To the mixture 15 mL of deionized water was added and then the mixture was poured into a 170 mL Teflon^{TM}-lined steel autoclave. The autoclave was then placed in a preheated convection furnace pre-set to 140 °C for 10 h.

After cooling the product was washed with deionized water until a neutral pH was reached followed by washing with ethanol. The powder was dried in a furnace at 80 °C for several hours.

NiO-synthesis

An aqueous 1.3 mM solution of $Ni(NO_3)_2 \cdot 6H_2O$ (Sigma Aldrich, ≥97.0%) was prepared and added dropwise to a 1.3 mM solution of citric acid until a ratio of 1:1 between $Ni(NO_3)_2$ and citric acid under constant stirring with pH = 1. The light green solution was heated on a heating plate and left overnight at 95 °C to dry the formed gel. The dried powder was afterwards milled and calcined at 400 °C with a slow heating rate of 1 °C/h with a holding time for 4 h before cooling to room temperature. The ratio between the starting compounds, pH-choice, calcination temperature and heating rate were based on the article by Wu *et al.*[25] to obtain small nanocrystallites of NiO.

2.2 Pellet preparation

The $Sr(Ni_{1-x}Zn_x)_2Fe_{16}O_{27}$ (x = 0, 0.5, 1) samples, in the following, referred to as Ni-p-1300 °C, NiZn-p-1300 °C and Zn-p-1250 °C, were prepared by mixing the prepared precursors powder of α-FeOOH and NiO with $SrCO_3$ (Strem Chemicals, 99.9%), ZnO (Alfa Aesar, 20-30 nm APS nanopowder, 99%) using a pestle and mortar. The powders were mixed using an excess of Sr.

To ensure the obtained molar ratios X-Ray Fluorescence (XRF) measurements were conducted for the mixed loose powders using a Rigaku NEX CG spectrometer. Powders were placed on a 6.0-micron polypropylene film with a powder depth of 1 mm. The final ratios for the powders for x = 0, 0.5 and 1 were (nZn+nNi+nFe)/nSr = 16.8, 17.5, 16.8 respectively all with excess strontium before calcination.

The powders were cold compacted into 6 mm pellets of 0.1 g with a pressure of 2.5 ton applied for 5 min. The pellets were then calcined in a furnace at 1250 °C for Zn-p-1250 °C or 1300 °C for NiZn-p-1300 °C and Ni-p-1300 °C with a heating rate of 600 °C/h and a holding time of 0 min before cooling to room temperature. Lower temperatures of 1200 °C and 1250 °C for calcination was tested, here larger amounts of impurities were seen. Powder diffraction patterns of the lower temperatures can be found in S1-3 and will not be described further.

2.3 CHARACTERIZATION AND DATA TREATMENT

Magnetic measurements

The magnetic properties of the pellets were measured with a Quantum Design, Physical Property Measurement System (PPMS) equipped with a vibrating sample magnetometer (VSM). For the magnetisation measurements of the pellets, the pellet was placed in a tubular brass sample holder and held between two quartz rods and the magnetic field was swept from ±3 T at 300 K.

In-house X-ray diffraction

Structural and microstructural characterization of the as-prepared starting materials and the pellets were carried out by X-ray powder diffraction equipped with a Co source (Rigaku SmartLab diffractometer. Rigaku, Japan).

The powder diffraction data were analyzed by Rietveld refinement using the FullProf Suite software package.[26] The zero-point correction, Chebychev polynomial background parameters, scale factors, and lattice parameters were refined for all samples.

Goethite, α-FeOOH, is described with the space group *Pnma*: a = 9.9564(2) Å, b = 3.0237(1) Å, c = 4.6104(2) Å. The broadening was refined using the fourth order spherical harmonics expansion of the crystallites shape model using Laue Class *mmm* and by refining the strain through the *X*-parameter.

For the refinement of NiO, NiO is described in the space group *Fm*-3*m:* $a = b = c$ = 4.1800(2)Å, the broadening was described using the Lorentzian crystallite size parameter *Y*.

Regarding the peak broadening of the pellets, it was either refined using the *Y* parameter or fixed to 0, the preferred orientation is described by the Modified March Dollase model[27,28] where a texture axis is defined parallel to the surface normal, and the G_1 parameter is refined.

Quantitative texture analysis

The three pellets were investigated at the synchrotron X-ray beamline P02.1 at PETRA-III, DESY, Hamburg in Germany, to gain information about structure, size, and texture. The 2D diffraction images were collected in transmission mode using a Perkin Elmer amorphous silicon detector and a wavelength of λ = 0.20709 Å. For each pellet, four images were collected at the ω angles = 0°, 15°, 30°, and 45°. The wavelength, sample to detector distance, and instrumental contribution to the peak broadening were determined by calibration with a NIST LaB_6 660B standard. The 2D images were imported into MAUD 2.97[22] using ImageJ[29] integrating azimuthally into 10° sections giving a total of 36*4 = 144 1D patterns that were simultaneously refined. The choice of a 10° integration step was to reduce the impact of spottiness seen in the diffraction images, see Figure S4. In MAUD polynomial background parameters, scale-factors, lattice parameters, and texture were refined using the E-WIMV model with a cell size = 10° and no symmetry imposed.

All MAUD-generated pole figures were loaded into MTEX 5.6.1,[30] which offers a wider possibility for plotting pole figures. In MTEX an ODF is generated from the MAUD-pole figures and then pole figures are visualized and texture indices are extracted from MTEX.

3 RESULTS AND DISCUSSION

3.1 Precursors

α-FeOOH

The powder diffraction pattern for the precursor is shown in Figure 2. The figure shows that the goethite sample is phase pure. The size refinement shows that the crystallites have a lathlike shape. With the smallest dimension along the *c*-axis 11.0 nm, while the size along the *a*-axis was 23.3 nm, and the largest dimension of 40.1 nm along the *b*-axis. In the model isotropic strain is accounted for and the apparent max-strain is 4.46%%. Comparison of results from PXRD, TEM, and STEM in other studies have shown that the formed goethite crystallites are aggregated, where the aggregation is primarily in the *b*-direction making the particle sizes appear significantly longer along this direction compared with the crystallite sizes extracted from powder diffraction, the aggregation is primarily observed in lower temperature syntheses.[31,32]

NiO

Almost phase-pure (96.9(4) wt.%) NiO crystallites are obtained through the synthesis with a small impurity of elemental Ni. In Figure S5 powder diffraction pattern and TEM images are presented along with size analysis. The crystallites appear spherical with sizes D_{PXRD}=5.9(1) nm and mean D_{TEM}=8.79 nm standard deviation (SD) = 2.39 nm, extracted from 269 particles.

As the amount of goethite is dominating compared to the amount of ZnO and NiO in the samples, it is expected that the final product will be texturized as seen in a similar study of MHF by Thomas-Hunt *et al.* where higher goethite content led to high texture index.[20]

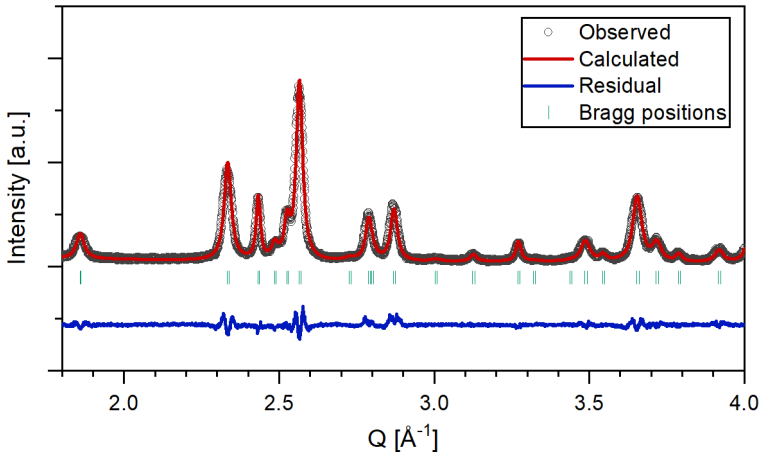

Figure 2: PXRD diffraction pattern of the precursor α-FeOOH. The dark grey circles indicate the experimental data, the red line represent the calculated Rietveld Model, the blue line represent the residual and Bragg positions are represented with green.

3.2 Calcined pellets

Magnetic properties at Room Temperature

The magnetic hysteresis curves of the three samples are shown in Figure 3 and the numeric values of M_s obtained by law of approach to saturation, and wt.% corrected M_s is given in table 1.

Saturation magnetisation

The hysteresis loops reveal relative high saturation magnetisations (M_s) for the Zn-p-1250 °C and NiZn-p-1300 °C samples with values of 78.19(2) Am^2kg^{-1} and 79.35(2) Am^2kg^{-1}, respectively. The samples contain some minor impurities, which are contributing additional mass and magnetisation to the measured samples. To obtain the intrinsic value of saturation magnetisation for the compounds $Sr(Ni_{1-x}Zn_x)_2Fe_{16}O_{27}$ ($x = 0$, 0.5, 1) the corrected saturation magnetization is reported in Table 1 along with the wt.% of the phases present. These corrections are described by Mørch *et. al.*[14] The weight fractions were extracted from the 2D Rietveld of the refinements of the synchrotron diffraction data, which will be described in detail below.

Coercivity

All samples show no appreciable H_c, <6 kAm^{-1}, this can be attributed to two different effects: 1) superparamagnetism or 2) large crystallites splitting into multiple magnetic domains. The 2D diffraction pattern is very spotty, pointing to very large crystallites, see supporting information Figure S4.

Remanence to saturation magnetization ratio

The squareness ratio M_r/M_s for all samples is low. This is a consequence of no appreciable H_c. The M_r/M_s does not provide a good measure of the preferred orientation in cases where the sample consists of large crystallites. The steep increase and quick plateauing in the hysteresis loop for the samples are an indication that the magnetic easy axis is pointing along the applied magnetic field direction. In other words, the samples show a high degree of preferred crystallographic orientation also known as texture. The insert in Figure 3 shows the first quadrant of the hysteresis loop normalized to the saturation magnetization of the respective samples, this makes it possible to compare the increase and plateauing of the three hysteresis loops. It can be deduced that the sample Ni-p-1300°C reaches saturation at lower field compared with NiZn-p-1300°C and Zn-p-1250°C, this indicates that the crystallites in Ni-p-1300°C have a higher degree of texture.

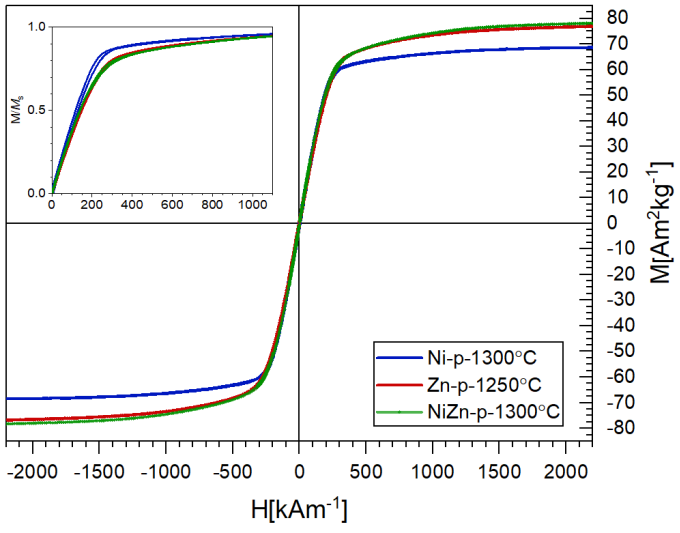

Figure 3: Magnetic hysteresis for the three samples. The samples were measured using an applied field of ±3 T at a temperature of 300 K with a PPMS-VSM. The insert shows the normalized magnetization using M_s.

$SrNiZnFe_{16}O_{27}$ and $SrZn_2Fe_{16}O_{27}$ show a significantly higher M_s than the maximum obtainable M_s for $SrFe_{12}O_{19}$ (74 Am^2kg^{-1}) and a fully aligned $SrZn_2Fe_{16}O_{27}$ could reach a hypothetical BH_{max} of 65 kJ/m^3 assuming $M_r = M_s$ and $H_c > ½M_s > 228$ kA/m. Confirming the that W-type hexaferrites indeed are interesting in the search for new and stronger permanent magnets, given that Zn does not significant change the anisotropy constant (K_1) and that the size of the crystallites and high degree of texture can be controlled.

	WHF (wt.%)	SF (wt.%)	M_s (Am^2kg^{-1})	$M_{s\ corrected}$ (Am^2kg^{-1})	H_c (kAm^{-1})
Zn-p-1250°C	92.71(3)	7.29(3)	78.19(2)	84.26(3)	2.7(1)
NiZn-p-1300°C	90.98(3)	9.02(3)	79.35(2)	79.71(4)	2.2(1)
Ni-p-1300°C	95.28(3)	4.72(3)	69.65(2)	70.61(3)	5.4(1)

Table 1: The table is showing weight fractions of the phases present extracted from MAUD-refinement of synchrotron data, M_s, H_c, and the $M_{s\ corrected}$ is corrected for the contribution from the spinel ferrite (SF). M_s used for $ZnFe_2O_4$, $Ni_{0.5}Zn_{0.5}Fe_2O_4$, $NiFe_2O_4$ corrections are 1 Am^2kg^{-1},[33] 75.72 Am^2kg^{-1},[34] 50 Am^2kg^{-1} [35], respectively.

The obtained saturation magnetisation values correspond very well with the results reported in the literature, Mørch *et al.* found $SrZn_2Fe_{16}O_{27}$ and $SrNi_2Fe_{16}O_{27}$ have saturation magnetisations of values 80.4(3) and 69.0(3) Am^2/kg, respectively.[14] Likewise did J.-H. You *et al.* find a M_s of 77.3(2) Am^2kg^{-1} for $SrZn_2Fe_{16}O_{27}$ in the study of the composition range $SrZn_xFe_{18-x}O_{27}$, while the highest saturation was found for $x = 1$ with a value of 87.7(5) Am^2kg^{-1}.[36] The samples reported by J.-H. You *et al.* also have vanishing coercivity with values between 7.2-9.5 kAm^{-1}. The highest reported M_s for W-type hexaferrite attains M_s = 91 Am^2kg^{-1} at room temperature for $SrZnLi_{0.5}Fe_{16.5}O_{27}$,[13] while highest H_c in W-type hexaferrites have been reported for $Sr_{0.9}Ca_{0.1}Zn_2Fe_{16}O_{27}$ with a H_c = 290.5 kAm^{-1}.[15]

In-house data collection

Diffraction data sets were collected for the calcined pellets using a Rigaku Smartlab, see Figure 4.

Preferred orientation: The observed patterns show clear preferred orientation of the W-type hexaferrite, which is observed as suppression of the (*hk*0) reflections, while (00*l*) reflections are enhanced in intensity. In Figure 4 there is a large discrepancy between the calculated intensity from the Rietveld

model and the observed intensity, this indicate that the texture is not described properly with the simple modified March model. Especially (1 0 9) (1 0 10) and (1 0 11) reflections are not well described as the calculated intensity is underestimated, this is also seen in the high R_{wp}-values, see Table 2. This could also be due to the relatively large crystallite grains constituting the sample resulting in poor powder statistics. The inadequate description of data along with undescribed peak intensities makes extractions of reliable phase fractions untrustworthy. The data can still provide a qualitative determination of the phases, preferred orientation, and the unit cell parameters.

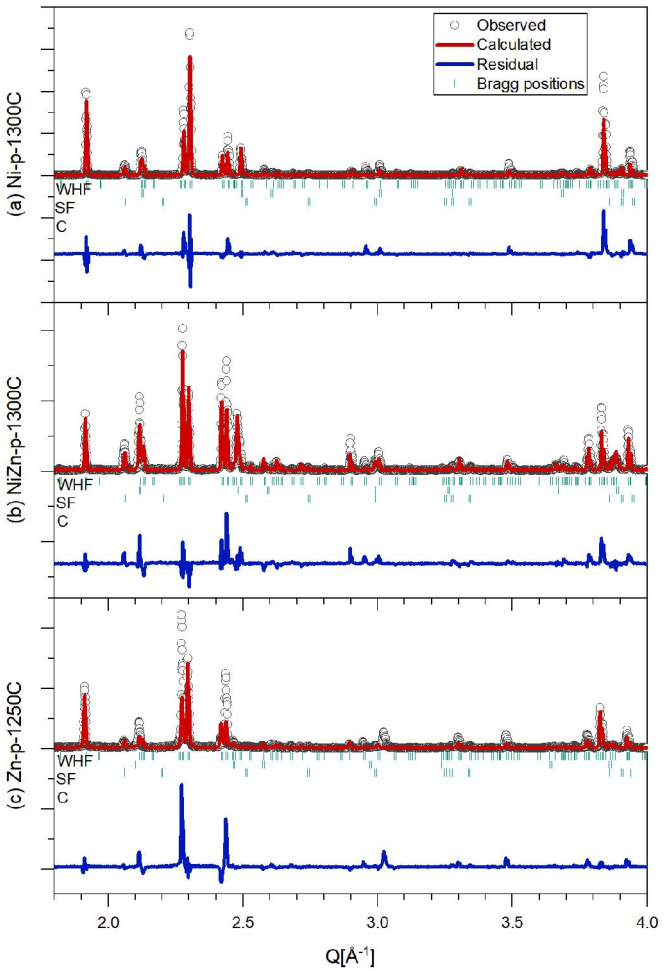

Figure 4: PXRD diffraction pattern of all samples a) Ni-p-1300°C, b) NiZn-p-1300°C and c) Zn-p-1250°C. The grey circles indicate the experimental data, the red line represent the calculated Rietveld Model, the blue line represent the residual and Bragg positions are represented with green for the three phases, WHF, SF and C ($CaCO_3$).

Phase identification: The major phase present in all the samples is the WHF alongside a minor secondary phase of spinel ferrite (SF), $Zn_{1-x}Ni_xFe_2O_4$. Additionally, scattering from $CaCO_3$ described in

space group *R*-3*c* is observed in all samples, this stems from plasticine used for mounting the sample *i.e.* the $CaCO_3$ is not in the sample. Undescribed peaks can be seen in the diffraction pattern for Zn-p-1250°C the positions of these are presented in S4 indicating the presence of another phase. These peaks are not seen in Ni-p-1300°C and NiZn-p-1300°C, the poor description of data as well as the weak intensity of the impurity peaks, has made it impossible to identify and characterize these minority phases in the samples.

Unit cell parameter: The unit cell parameters extracted for the refinement of the phases are given in Table 2. The unit cell parameters decrease for both WHF and SF with the increasing Ni-content, this can be understood when comparing ionic radii: Zn^{2+} has larger radius (60 pm in tetrahedral, 74 pm in octahedral coordination[37]) compared to Ni^{2+} (55 pm in tetrahedral, 69 pm in octahedral[37]) and both have a larger radius than Fe^{3+} (49 pm in tetrahedral, 64.5 pm in octahedral[37]), therefore the trend is a clear indication of increasing incorporation of Ni into the structure. The present data cannot reveal anything about the coordination of Zn, Ni and Fe in the structure as the elements are next nearest neighbours in the periodic table. For the spinel ferrite phase, there is likewise a decrease in unit cell parameters when increasing the Ni content in the samples, indicating the spinel in NiZn-p-1300°C contains both Zn and Ni in the structure.

	Rigaku Smartlab, Fullprof				P02.1, PETRAIII, MAUD			
	WHF		SF	R_{wp} (%)	WHF		SF	R_{wp} (%)
	a=*b* (Å)	*c* (Å)	*a*=*b*=*c* (Å)		*a*=*b* (Å)	*c* (Å)	*a*=*b*=*c* (Å)	
Zn-p-1250°C	5.9013(1)	32.8390(7)	8.4604(1)	42.5	5.90927(1)	32.8800(2)	8.4641(1)	16.18
NiZn-p-1300°C	5.8959(1)	32.7928(5)	8.4028(2)	31.3	5.90043(2)	32.8200(4)	8.4055(1)	19.13
Ni-p-1300°C	5.8898(1)	32.7288(5)	8.3601(1)	38.0	5.89443(2)	32.7837(5)	8.3694(1)	18.97

Table 2: Unit cell parameters along with the R_{wp}-parameters from the refinement of data collected from both the Rigaku Smartlab Diffractometer and at P02.1, PETRAIII

Synchrotron data collection

Figure 5 shows 2D diffraction plots for Ni-p-1300°C sample collected at ω = 45°. The residual shows a good agreement between the observed and calculated diffraction pattern. This is also the case for NiZn-p-1300°C and Zn-p-1250°C see Figure S8-9. Similar agreements are seen for the other angles ω = 0°,

15°, 30° for all samples. The R_{wp} values presented in Table 2 for the synchrotron data are significantly lower for the three refinements compared with in-house diffraction. The refinements reveal similar trends in unit cell parameters as seen in refinements of the in-house collected data. The refined peak broadening is out of resolution indicating large crystallites >200 nm.[38] Due to the more comprehensive data collection and a more sophisticated refinement model, quantitative information of weight fractions and texture information can be obtained more reliably compared to in-house diffraction.

Phase identification and weight fractions: W-hexaferrite is observed as the major phase, while a minor impurity of a $Zn_{1-x}Ni_xFe_2O_4$ is observed in all three pellets. This corresponds to what was determined using the in-house Rigaku Smartlab. The weight fractions are given in Table 1. The weight fraction of WHF is 92-95% in all samples. For Zn-p-1250°C the undescribed peaks observed in the in-house data are no longer observed in the sample, the undescribed peaks could be the result of an impurity present at the surface. A detailed study of the phase stability was reported by J.-H. You *et al.*[39]

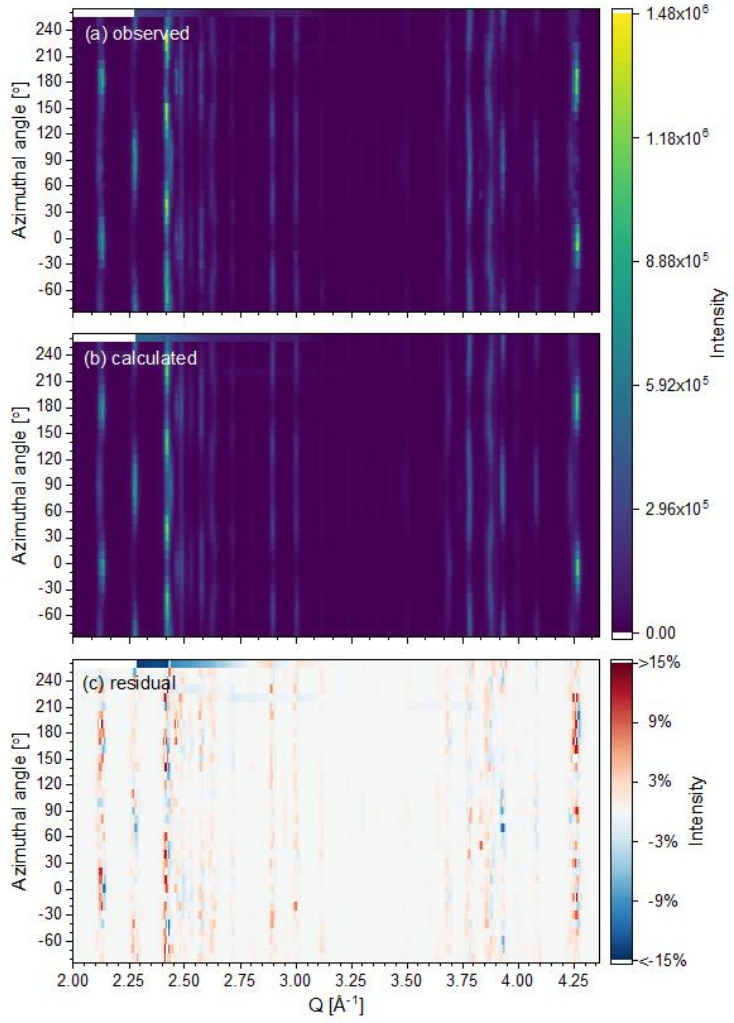

Figure 5: 2D diffraction data refinement of sample Ni-p-1300°C for an ω angle of 45°, with the scattering vector Q [Å^{-1}] along the x-axis, the azimuthal angle η [°] along the y-axis and intensity as the colormap. a) shows the observed data, b) the calculated model, and c) the residual. Linear scaling is used in the plots while the perceptually linear colormap cividis[40] has been chosen for data visualization. The difference plot is shown on a scale ±15%, where the max deviation was 29.6%.

Full texture analysis: In Figures 5a and 5b, the observed and calculated pattern for Ni-p-1300°C ω = 45° is shown. The texture is observed in the patterns as the intensity of a reflection varies along the azimuthal angle. Figure 5c shows the residual between the observed data (Figure 5a) and the model (Figure 5b), the residual indicates an overall good agreement between the observed data and the model *i.e.,* the model is giving a good structural description of the texture. The discrepancies observed in specific areas are believed to be connected to the spottiness of the observed data due to large crystallites in the sample.

In Figure 6 the three recalculated pole figures for the (008) reflection for the three samples can be seen. All samples show a preferred orientation where the (00*l*) axis in the crystal structure aligns with the surface normal of the pressed pellet. The most textured sample is Ni-p-1300°C as clearly seen from the reconstructed pole figure, while NiZn-p-1300°C has the least texture.

The texture index extracted from the texture model in the MTEX software is given below the pole figures in Figure 6. The obtained texture indices are all above 1.00, the value for a perfectly randomly oriented sample.[41]

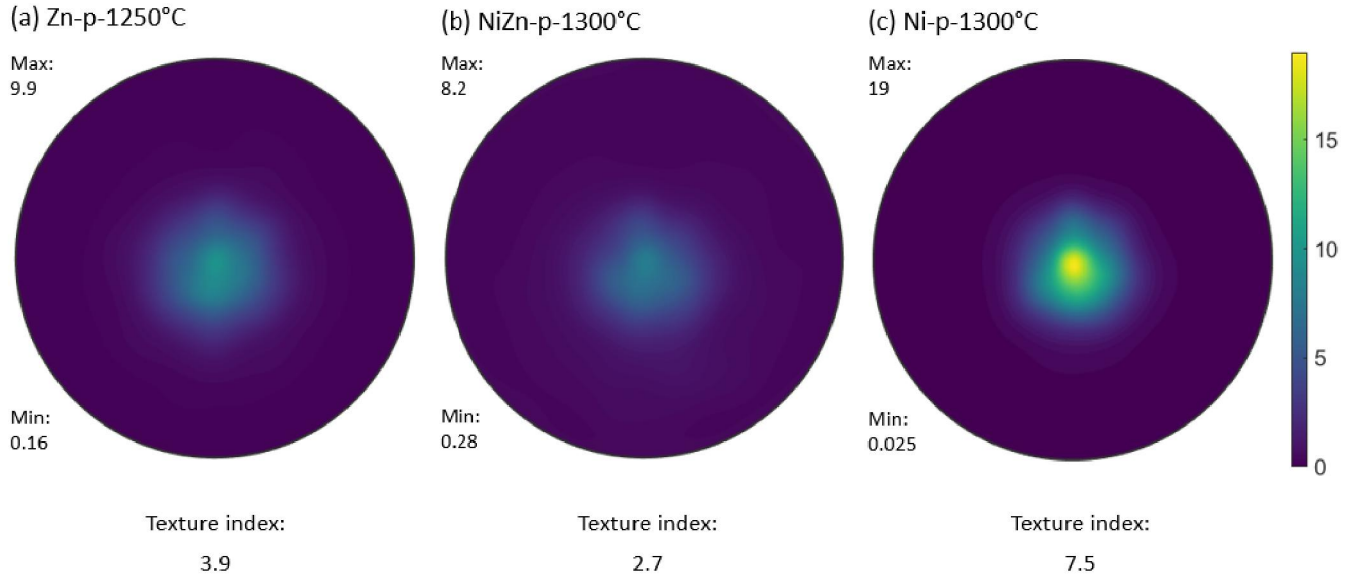

Figure 6: Reconstructed (008) pole figures for all samples. The scaling of the color bar to the right in the figure applies to all pole figures. The min. and max. value for the pole figures has been given to the left of each pole figure and the texture indices are given below the pole figures.

The reason for the variation in texture indices between the samples Zn-p-1250°C, Ni-p-1300°C, and NiZn-p-1300°C is not clear. It could be related to the size and reactivity of the ZnO and NiO nanoparticles as well as it could be correlated to the content of spinel impurity. Time and temperature also play a role in aligning the crystallites. Longer sintering time and higher temperatures have earlier been revealed to increasing the preferred orientation as well as affect the crystallite sizes. It is seen that preferred orientation is improved with longer sintering times, as the grains with a preferred orientation grow at the expense of non-oriented grains in the sample.[42]

Earlier studies of the preservation of preferred orientation through a phase transition have also been reported elsewhere, where a study has been done on the transition from MHF to WHF. In the study the MHF particles were oriented in a magnetic field alongside SF and the orientation is seen to be preserved through the transition to WHF.[19]

This preservation of preferred orientation through related structures is also believed to be the origin of the preferred orientation of WHF reported here for Ni-p-1300°C, NiZn-p-1300°C and Zn-p-1250°C. The texture is believed to be created by the use of the non-magnetic interacting anisotropic shaped goethite particles allowing for alignment of particles without the use of a magnetic field. The orientation is preserved through multiple phase transitions between the structures, that are closely related and all having the closed packed oxygen layers perpendicular to the *c*-axis direction. This is also seen for aligned samples of MHF, where non-magnetic and anisotropic-shaped crystallites of goethite and sixline-ferrihydrite result in high texture indices and high M_r/M_s.[20,21,43]

Table 3 list the comparison of M_r/M_s to texture indices for aligned hard M-type hexaferrites magnets found within the existing literature. In general, it is clear that higher texture indices correspond to higher M_r/M_s values, however the sample presented with the highest texture index is not the sample with the highest M_r/M_s value. This could be a consequence of data treatment either by the corrections done to the collected magnetic measurements or potential differences in the texture description. It could also be a consequence of crystallite sizes, as the samples with the highest texture index also was exposed to the highest temperature / longest time during the spark plasma sintering (SPS). For single crystals of MHF it is seen that the samples have a no appreciable H_c nor M_r.[44] This is also what is observed for the samples of WHF.

Synthesis of the initial powders	Pressing technique and heating	Data collection, Texture model	M_r/M_s	Texture index (m.r.d.^{2})	Ref
Prepared α-FeOOH by AC mixed with $SrCO_3$	CC, T_{calc} =1150 °C, t_{hold} = 0 min	Transm. synchrotron measurement, EWIMV	0.83(1)	3.77	[20]
Prepared Sixline ferrihydrite and SrFe-amph. phase by AC	SPS: T_{max} = 750 °C, P_{max} = 100 MPa t_{hold} = 2 min	Transm. synchrotron measurement, EWIMV	0.93	11.1	[43]
MHF by FL	SPS: T_{max} = 1000 °C, P_{max} = 100 MPa t_{hold} = 2 min	XPF, MTEX	0.883(6)	17.23	[45]
MHF by AC	SPS: T_{max} = 900 °C, P_{max} = 100 MPa t_{hold} = 2 min	XPF, MTEX	0.90	7.40	[46]
MHF by FL	As above	XPF, MTEX	0.81	3.21	
MHF by MSG	As above	XPF, MTEX	0.74	1.68	
MHF by SG	As above	XPF, MTEX	0.56	1.09	
MHF by AC, pre-aligned in a magnetic field	SPS: T_{max} = 950 °C, P_{max} = 100 MPa t_{hold} = 5 min	XPF, MTEX	0.887(2)	19.15	[11]

Table 3: Table comparing M_r/M_s and texture indices for differently prepared samples of hard M-type hexaferrites. Samples compacted by either Spark Plasma Sintering (SPS) or cold compaction (CC). Samples prepared by different synthesis methods: sol–gel (SG), modified sol–gel (MSG), supercritical hydrothermal continuous flow (FL) and hydrothermal autoclave (AC) synthesis.

If size-control can be managed and integrated in this synthesis route it is believed that the WHF samples would also show high M_r/M_s, which is the general trend seen in Figure 7. A texture index of 7.5 could potentially lead to an M_r/M_s between 0.83 and 0.90. The WHF has an improved M_s compared with MHF and controlling texture formation is an important step closer towards realizing permanent magnets of WHF, it only leaves the final step to increase H_c.

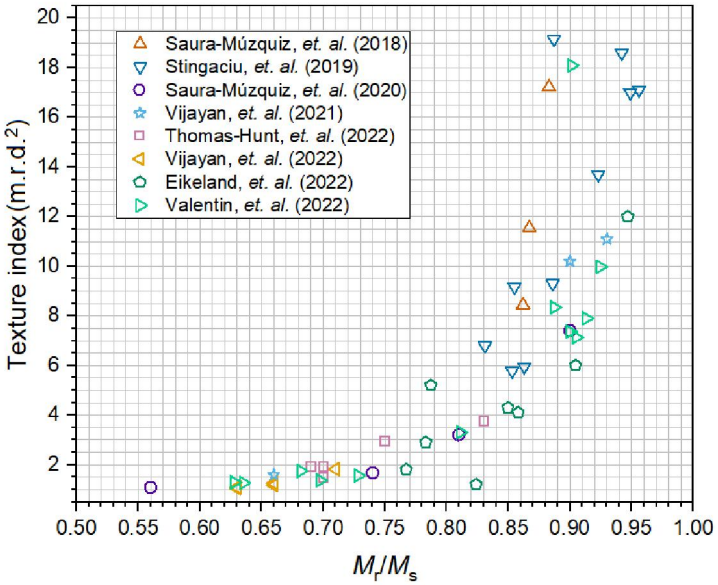

Figure 7: Texture index related to M_r/M_s for differently prepared samples of hard M-type hexaferrites found in the literature.[11,20,21,43,45–48] Specific details such as synthesis condition, pressing technique and texture model are presented for some of the samples in Table 3.

The advantage of using anisotropically shaped nanocrystallites to cause crystallographic preferred orientation is not limited to permanent magnets. The method may be advantageous in other materials research fields where directional properties are important *e.g.* thermoelectrics, piezoelectrics, superconductors, batteries, etc. The preparation of highly textured WHF demonstrate a novel approach to optimization and targeted design of advanced functional materials.

4 CONCLUSION

We show that the use of non-magnetic interacting, anisotropic-shaped, goethite particles can be used to create almost phase pure W-hexaferrite samples with a preferred orientation in the final magnets without the use of an applied external magnetic field. This is a simple, easy, and green solution, suitable for industry applications. The saturation magnetization M_s revealed that the hypothesis that W-type hexaferrite can produce magnets with higher saturation magnetization M_s compared with M-type is correct. The M_s for the samples Zn-p-1250 °C, NiZn-p-1300 °C were measured to be 78.19(2) and 79.35(2) Am^2kg^{-1}, respectively. If corrected for the known impurity of spinel the saturation magnetization of Zn-p-1250°C reached 84.26(3) Am^2kg^{-1}. The results reveal that M_r/M_s is not a sufficient measure for texture when the samples have low coercivity, here H_c <6 kAm^{-1}. To characterize the samples in more detail a full texture synchrotron analysis was performed, where texture was observed aligning (00*l*) with the pellet normal and texture indexes of 3.9, 2.7, and 7.5 m.r.d.[2] for Zn-p-1250 °C, NiZn-p-1300 °C, and Ni-p-1300 °C, respectively, underlining that texture is created in all samples. If this formation of texture can be controlled, while increasing coercivity H_c it could lead to high M_r/M_s and in turn the potential to have larger energy product (BH_{max}) compared to M-type hexaferrites $SrFe_{12}O_{19}$.

5 CONFLICTS OF INTEREST

There are no conflicts to declare.

6 ACKNOWLEDGMENTS

This work was financially supported by the Innovation Fund Denmark (MAGFLY 7046-00015B) and the Independent Research Fund Denmark - Green Transitions COMPASS (1127-00235B). We thank the Danish Agency for Science, Technology, and Innovation for funding the instrument center DanScatt (7129-00003B) supporting access to beamtime. Parts of this research were carried out at PETRA-III at DESY, a member of the Helmholtz Association (HGF). We would like to thank Alexander Schokel and Frederik H Gjørup for assistance in using beamline P02.1. Affiliation with the ESS lighthouses SMART and Q-MAT as well as the Center for Integrated Materials Research (iMAT) at Aarhus University is gratefully acknowledged.

7 REFERENCES

1 F. Jimenez-Villacorta and L. H. Lewis, in *Nanomagnetism*, One Central Press, 2014.

2 O. Gutfleisch, M. A. Willard, E. Brück, C. H. Chen, S. G. Sankar and J. P. Liu, *Adv. Mater.*, 2011, **23**, 821–842.

3 R. C. Pullar, *Prog. Mater. Sci.*, 2012, **57**, 1191–1334.

4 B. M. Kirrane, L. S. Nelson and R. S. Hoffman, *Basic Clin. Pharmacol. Toxicol.*, 2006, **99**, 358–359.

5 M. M. Bomgardner, *Chem. Eng. News*, 2015, **93**, 36–39.

6 J. Wübbeke, *Resour. Policy*, 2013, **38**, 384–394.

7 F. H. Gjørup, M. Saura-Múzquiz, J. V. Ahlburg, H. L. Andersen and M. Christensen, *Materialia*, 2018, **4**, 203–210.

8 G. C. Hadjipanayis, *J. Magn. Magn.*, 1999, **200**, 373–391.

9 E. C. Stoner and E. P. Wohlfarth, *Philos. Trans. Royal Soc.*, 1948, **240**, 599–642.

10 A. Z. Eikeland, M. Stingaciu, A. H. Mamakhel, M. Saura-Múzquiz and M. Christensen, *Sci. Rep.*, 2018, **8**, 7325.

11 M. Stingaciu, A. Z. Eikeland, F. H. Gjørup, S. Deledda and M. Christensen, *RSC Adv.*, 2019, **9**, 12968–12976.

12 H. Kojima, in *Handbook of Ferromagnetic Materials*, North-Holland, 1982, vol. 3, pp. 305–391.

13 S. Ram and J. C. Joubert, *J. Magn. Magn.*, 1991, **99**, 133–144.

14 M. I. Mørch, J. v. Ahlburg, M. Saura-Múzquiz, A. Z. Eikeland and M. Christensen, *IUCrJ*, 2019, **6**, 492–499.

15 S. Ram and J. C. Joubert, *IEEE Transactions on Magnetics*, 1992, **28**, 15–20.

16 G. Litsardakis, D. Samaras and A. Collomb, *J. Magn. Magn.*, 1989, **81**, 184–188.

17 Y. Wang, Y. Liu, X. You, S. Liu, C. Wu, Q. Liu, H. Zhang and V. G. Harris, *J. Alloys Compd.*, 2019, **772**, 1100–1104.

18 Q. Liu, T. Ben, L. Chen and L. Jing, *J. Eur. Ceram. Soc.*, 2021, **41**, 7717–7722.

19 F. K. Lotgering, *J. Inorg. Nucl.*, 1959, **9**, 113–123.

20 J. Thomas-Hunt, A. Povlsen, H. Vijayan, C. G. Knudsen, F. H. Gjørup and M. Christensen, *Dalton Trans.*, 2022, **51**, 3884–3893.

21 H. Vijayan, A. Povlsen, J. Thomas-Hunt, M. I. Mørch and M. Christensen, 2022, *J. Alloys Compd.*, 2022, **915**, 165333

22 L. Lutterotti, M. Bortolotti, G. Ischia, I. Lonardelli and H.-R. Wenk, *Z. Kristallogr. Suppl.*, 2007, **26**, 125–130.

23 S. Matthies and G. W. Vinel, *Phys. Status Solidi B*, 1982, **112**, K111–K114.

24 K. Momma and F. Izumi, *J. Appl. Crystallogr.*, 2011, **44**, 1272–1276.

25 Y. Wu, Y. He, T. Wu, T. Chen, W. Weng and H. Wan, *Mater. Lett.*, 2007, **61**, 3174–3178.

26 J. Rodríguez-Carvajal, *Phys. B Condens. Matter*, 1993, 192, 55–69.

27 A. March, *Z. Kristallogr. Cryst. Mater*., 1932, **81**, 285–297.

28 W. A. Dollase, *J. Appl. Crystallogr.*, 1986, **19**, 267–272.

29 C. A. Schneider, W. S. Rasband and K. W. Eliceiri, *Nat. Methods*, 2012, **9**, 671–675.

30 F. Bachmann, R. Hielscher and H. Schaeben, *Solid State Phenom.*, 2010, **160**, 63–68.

31 P. J. Heaney, M. J. Oxman and S. A. Chen, *Am. Mineral.*, 2020, **105**, 652–663.

32 R. M. Cornell and U. Schwertmann, *The Iron Oxides: Structure, Properties, Reactions, Occurrences and Uses*, Wiley, 2., 2006.

33 B. Jeyadevan, K. Tohji and K. Nakatsuka, *J. Appl. Phys.*, 1994, **76**, 6325–6327.

34 A. S. Džunuzović, N. I. Ilić, M. M. Vijatović Petrović, J. D. Bobić, B. Stojadinović, Z. Dohčević-Mitrović and B. D. Stojanović, *J. Magn. Magn.*, 2015, **374**, 245–251.

35 A. Berkowitz, J. Lahut and C. VanBuren, *IEEE Trans. Magn.*, 1980, **16**, 184–190.

36 J.-H. You, S.-I. Yoo, *J. Alloys Compd.*, 2018, **763**, 459-465.

37 R. D. Shannon, *Acta Crystallogr. A*, 1976, **32**, 751–767.

38 C. Weidenthaler, *Nanoscale*, 2011, **3**, 792–810.

39 J. -H. You, H.-J. Kim, J.-W., Lee, S.-I. Yoo, *Mater. Sci. Eng. B*, 2022, **277**, 115563.

40 J. R. Nuñez, C. R. Anderton and R. S. Renslow, *PLOS ONE*, 2018, **13**, e0199239.

41 D. Chateigner, L. Lutterotti and M. Morales, in *International Tables for Crystallography*, 2019, vol. H, pp. 555–580.

42 F. K. Lotgering, *J. Inorg. Nucl.*, 1960, **16**, 100–108.

43 H. Vijayan, C. G. Knudsen, M. I. Mørch and M. Christensen, *Mater. Chem. Front.*, 2021, **5**, 3699–3709.

44 D. A. Vinnik, S. A. Gudkova, D. A. Zherebtsov, E. A. Trofimov, L. S. Mashkovtseva, A. v Trukhanov, S. v Trukhanov, S. Nemrava, B. Blaschkowski and R. Niewa, *J. Magn. Magn.*, 2019, **470**, 97–100.

45 M. Saura-Múzquiz, C. Granados-Miralles, H. L. Andersen, M. Stingaciu, M. Avdeev and M. Christensen, *ACS Appl. Nano Mater.*, 2018, **1**, 6938–6949.

46 M. Saura-Múzquiz, A. Z. Eikeland, M. Stingaciu, H. L. Andersen, C. Granados-Miralles, M. Avdeev, V. Luzin and M. Christensen, *Nanoscale*, 2020, **12**, 9481–9494.

47 A. Z. Eikeland, F. H. Gjørup, H. L. Andersen and M. Christensen, 2022, *Work in Progress*.

48 J. L. Valentin, F. H. Gjørup and M. Christensen, 2022, *Work in* ***Progress***.